

Theoretical structure factors for selected oxides and their effects in high-resolution electron-microscope (HREM) images

B. Deng and L. D. Marks*

Department of Materials Science and Engineering, Northwestern University, 2220 Campus Drive, Cook Hall 2036, Evanston, IL 60208-3108, USA. Correspondence e-mail: l-marks@northwestern.edu

A reasonably detailed analysis of the effects of charge redistribution on both X-ray and electron structure factors as well as for high-resolution electron-microscope images are presented for a series of light-element oxides. The charge redistribution leads to differences of 2–3% for the X-ray structure factors and 5–7% for electron structure factors in the 0–0.5 Å⁻¹ region. There are detectable changes in images of about 10% of the contrast, somewhat dependent upon the alignment of atom columns, specimen thickness and defocus. These studies suggest that charge redistribution may be detectable using a C_c -limited aberration-corrected microscope with a specimen thickness of about 50 Å.

© 2006 International Union of Crystallography
Printed in Great Britain – all rights reserved

1. Introduction

Theoretical X-ray and electron structure factors are essential for numerous crystallographic calculations, especially for structure refinements and electron-microscope image simulations. It is well known that X-ray structure factors are determined by the total ground-state charge density $\rho(\mathbf{r})$ in a crystal. Electron structure factors are also determined by $\rho(\mathbf{r})$, since swift electrons are diffracted by the Coulomb potential $\phi(\mathbf{r})$, which is related to $\rho(\mathbf{r})$ by Poisson's equation. The normal approach to structure factors is a Fourier summation of atomic scattering factors, which are either tabulated or fitted by a linear combination of Gaussian functions. The earliest atomic scattering factors were obtained from atomic charge-density calculations using the Hartree–Fock–Slater approach (Lieberman *et al.*, 1971). Later calculations considered relativistic effects (Doyle & Turner, 1968), which are quoted in *International Tables for Crystallography*, Vol. C (Madsen *et al.*, 1992), while more recent atomic scattering factors were derived from relativistic multiconfiguration Dirac–Fock calculations (Rez *et al.*, 1994).

All of the above scattering-factor calculations are based on a linear superposition of atomic charge densities, which neglects the redistribution of charge caused by crystal bonding. Since the nucleus and core electrons are largely unaffected by bonding, high-angle scattering factors should be well represented by a linear superposition. Therefore, the charge redistribution should primarily affect the low-order scattering factors. The error is reported to be ~1% for low-angle X-ray scattering factors and is usually acceptable for most calculations (Zuo *et al.*, 1997). Electron diffraction is more sensitive at small scattering angles and the low-angle

electron scattering factors change by ~5%. There is now a fairly extensive literature of experimental (electron) structure-factor measurements in bulk materials using quantitative convergent-beam electron diffraction techniques (Zuo *et al.*, 1988; Zuo & Spence, 1991; Gjonnes & Boe, 1994; Saunders *et al.*, 1995, 1996; Holmestad & Birkeland, 1998; Nuechter *et al.*, 1998; Holmestad *et al.*, 1999; Saunders *et al.*, 1999; Zuo *et al.*, 1999; Jiang *et al.*, 2002; Tsuda *et al.*, 2002; Jiang *et al.*, 2003; Zuo, 2004).

One important piece of analysis that, slightly surprisingly, has not attracted much attention to date is to analyze under what conditions one may expect to see substantial bonding effects in structure factors, particularly in electron diffraction. While there have been several cases where density functional theory (DFT) has been used to calculate structure factors which have been compared to electron diffraction data (Friis *et al.*, 2003; Zuo, 2004; Wu *et al.*, 2004; Zheng *et al.*, 2005), no attempt was made to investigate which zone axes have the highest sensitivity or to compare the trends across a range of materials in a reasonably systematic fashion. Going beyond this, an additional question is whether it is possible (now or in the future) to directly image the effects due to charge redistribution in a solid, and what level of accuracy would be required in images. The intention of this paper is to explore these two questions using density functional theory techniques. The first part of this paper evaluates charge redistribution effects on structure factors by comparing theoretical structure factors from a linear superposition of atomic charge densities and the crystal electron density calculated using density functional methods. The results we find are not particularly different from what has previously been found for simpler oxides. The second part focuses on the effects on high-

Table 1

Selected oxides containing Al, Si and Mg.

Chemical formula	Structure prototype	Z	Space group and unit-cell information
Al ₂ SiO ₅	Andalusite	4	<i>Pnmm</i> (No. 58), <i>a</i> = 7.876, <i>b</i> = 7.957, <i>c</i> = 5.566 Å
Mg ₂ SiO ₄	Forsterite	4	<i>Pnma</i> (No. 62), <i>a</i> = 10.190, <i>b</i> = 5.850, <i>c</i> = 4.790 Å
MgSiO ₃	Perovskite	4	<i>Pnma</i> (No. 62), <i>a</i> = 4.931, <i>b</i> = 6.908, <i>c</i> = 4.779 Å
Mg ₂ SiO ₄	Olivine	4	<i>Pnma</i> (No. 62), <i>a</i> = 10.207, <i>b</i> = 5.985, <i>c</i> = 4.754 Å
Al ₂ Mg ₃ Si ₃ O ₁₂	Pyrope	8	<i>Ia3d</i> (No. 230), <i>a</i> = 11.459, <i>b</i> = 11.459, <i>c</i> = 11.459 Å
Mg ₂ SiO ₄	Ringwoodite	8	<i>Fd3ms</i> (No. 227), <i>a</i> = 8.071, <i>b</i> = 8.071, <i>c</i> = 8.071 Å
Al ₂ SiO ₅	Sillimanite	4	<i>Pnma</i> (No. 62), <i>a</i> = 7.681, <i>b</i> = 5.777, <i>c</i> = 7.488 Å
Mg ₂ SiO ₄	Wadsleyite	8	<i>Imma</i> (No. 74), <i>a</i> = 11.680, <i>b</i> = 5.710, <i>c</i> = 8.160 Å

resolution electron-microscope images. We show that, similar to diffraction experiments, there are changes of the order of 5–15% in the image contrast due to bonding, which can in principle be directly observed.

2. Methods

2.1. Theoretical calculations of X-ray structure factors

As examples, we selected eight different oxides (see Table 1), all of which contain relatively light elements where one might expect to find experimentally observable effects due to bonding. Three different theoretical X-ray structure factors are included in this study. The first set, $F_{\text{fit}}^{\text{x}}$, is a conventional neutral-atom approach using a recent analytical form for the atomic scattering factors (Waasmaier & Kirfel, 1995) as a linear combination of five Gaussians:

$$f^{\text{x}}(s) = \sum_{i=1}^5 a_i \exp(-b_i s^2) + c, \quad (1)$$

where a_i , b_i and c are tabulated parameters and s is $\sin(\theta)/\lambda$. For these, and all other cases, the Debye–Waller factor B was held constant (0.25 Å²) for all atoms.

The second set ($F_{\text{sup}}^{\text{x}}$) was also a linear superposition of atomic densities using relativistic Dirac–Slater (DS) wavefunctions. The atomic charge densities from the DS method might vary slightly from those in the commonly used multi-configuration Dirac–Fock approach (Grant *et al.*, 1980).

The final set was calculated by (all-electron) density functional theory using the *Wien2k* program (Blaha *et al.*, 1990, 2001). These calculations were performed non-spin-polarized using the GGA exchange–correlation functional scheme (Perdew *et al.*, 1996). Muffin-tin radii of 1.5 atomic units (a.u.) were used for Mg or Al in olivine, pyrope, ringwoodite and wadsleyite. For all other atoms, the muffin-tin radii were 1.6 a.u. The numbers of k points in the Brillouin zone were varied to ensure convergence, typically 300–500. In all calculations, 781 radial mesh points were used to sample the muffin-tin spheres in the radial direction. For maximum angular momentum of the radial wavefunction, a value of $l_{\text{max}} = 10$ was used, and plane-wave cut-offs of $R_{\text{mt}}K_{\text{max}} = 7$, and $G_{\text{max}} = 14$ were used for expanding the charge densities and potentials. The X-ray structure factors, denoted here as $F_{\text{scf}}^{\text{x}}$, were obtained by Fourier transformation of the converged charge density in the muffin-tin spheres and interstitial region.

Table 2

Electron-microscope parameters for image simulations.

	Hitachi 9000	JEOL 2200FS-AC C _s -limited	JEOL 2200FS-AC C _c -limited
Accelerating voltage (kV)	300	200	200
Spherical aberration, C _s (mm)	0.9	−0.005	0.005
Beam convergence (mrad)	0.68	0.1	0.1
Defocus spread (Å)	80	40	40
Defocus (Å)	−490	35	−35
Defocus sampling (Å)	40	20	20

2.2. Theoretical calculation of electron structure factors

The atomic scattering factors for electrons [$f^{\text{e}}(s)$] were calculated from those for X-rays [$f^{\text{x}}(s)$] using the Mott–Bethe formula:

$$f^{\text{e}}(s) = \frac{m_0 e^2}{2h^2 s^2} [Z - f^{\text{x}}(s)] = 0.023\,933\,754 \frac{[Z - f^{\text{x}}(s)]}{s^2}, \quad (2)$$

where m_0 is the relativistically corrected electron mass, e is the electronic charge, h is Planck’s constant, Z is the atomic number, $f^{\text{x}}(s)$ is in electrons and $f^{\text{e}}(s)$ is in Å. To minimize errors arising from the use of equation (2) at small-angle scattering, a limiting form is used when s is small (Peng & Cowley, 1988); the value of $f^{\text{x}}(0)$ for the case when the structure factors were calculated by DFT was taken as the same as that for the tabulated Gaussian fits. This will lead to a small error in the mean inner potential but this has a negligible effect as it really only changes the overall phase of the exit wave. To be consistent, $F_{\text{fit}}^{\text{e}}$, $F_{\text{scf}}^{\text{e}}$ and $F_{\text{sup}}^{\text{e}}$ refer to the electron structure factors generated from $F_{\text{fit}}^{\text{x}}$, $F_{\text{scf}}^{\text{x}}$ and $F_{\text{sup}}^{\text{x}}$, respectively.

2.3. Multislice calculations

Image simulations were calculated by the well established multislice method (Cowley & Moodie, 1957; Goodman & Moodie, 1974). The potential of the whole unit cell was projected along the beam direction, then divided to give an effective potential for a single slice with a thickness of less than 2 Å. While this ignores higher-order Laue-zone (HOLZ) reflections, since HOLZ diffraction is predominantly at quite large angles, we can expect the effects to be small in the low-angle bonding-order regime. A conventional non-linear imaging code was then used to simulate the images for three

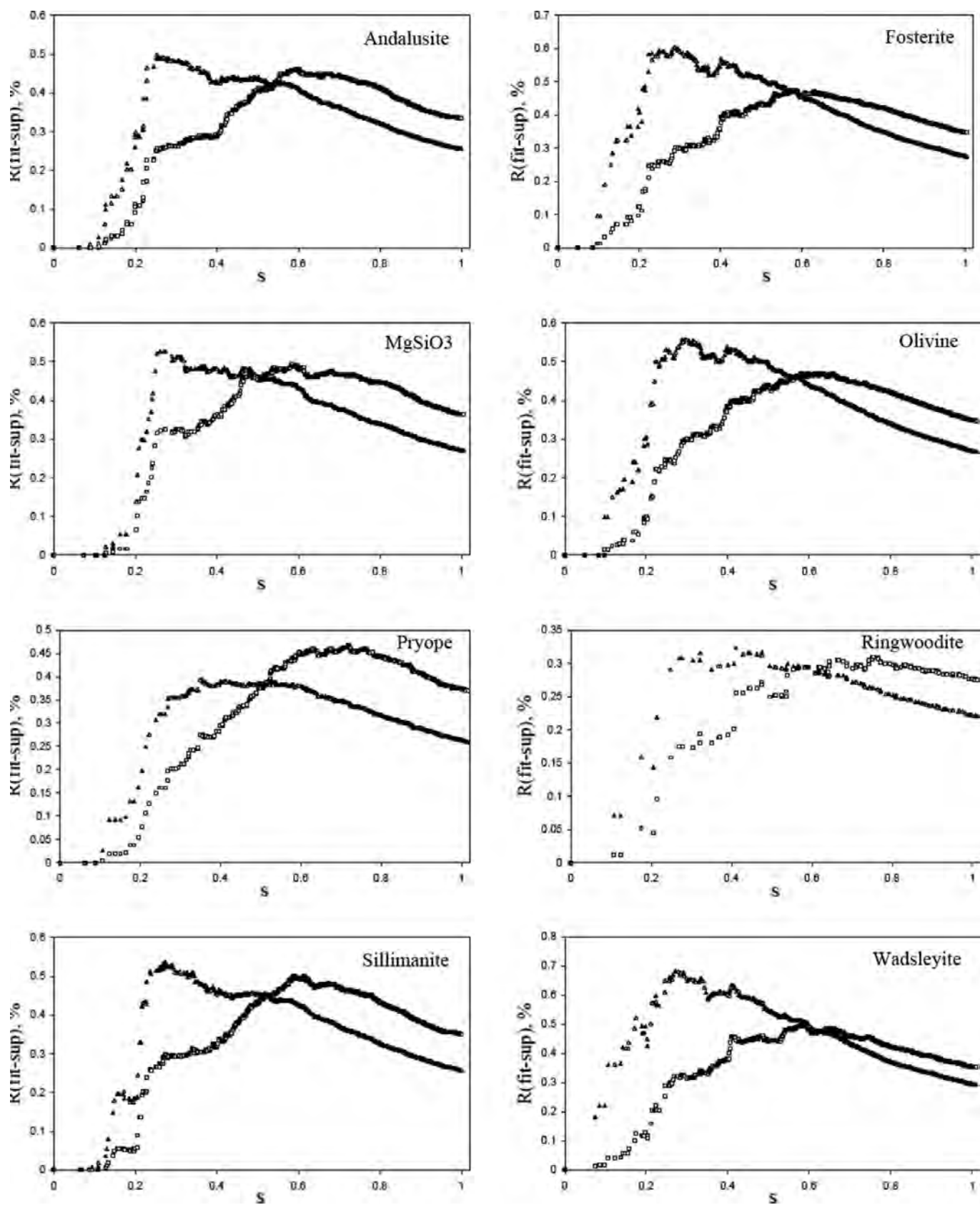


Figure 1
 $R(\text{fit-sup})$ for X-ray structure factors (squares) and electron structure factors (triangles). The unit of s is \AA^{-1} .

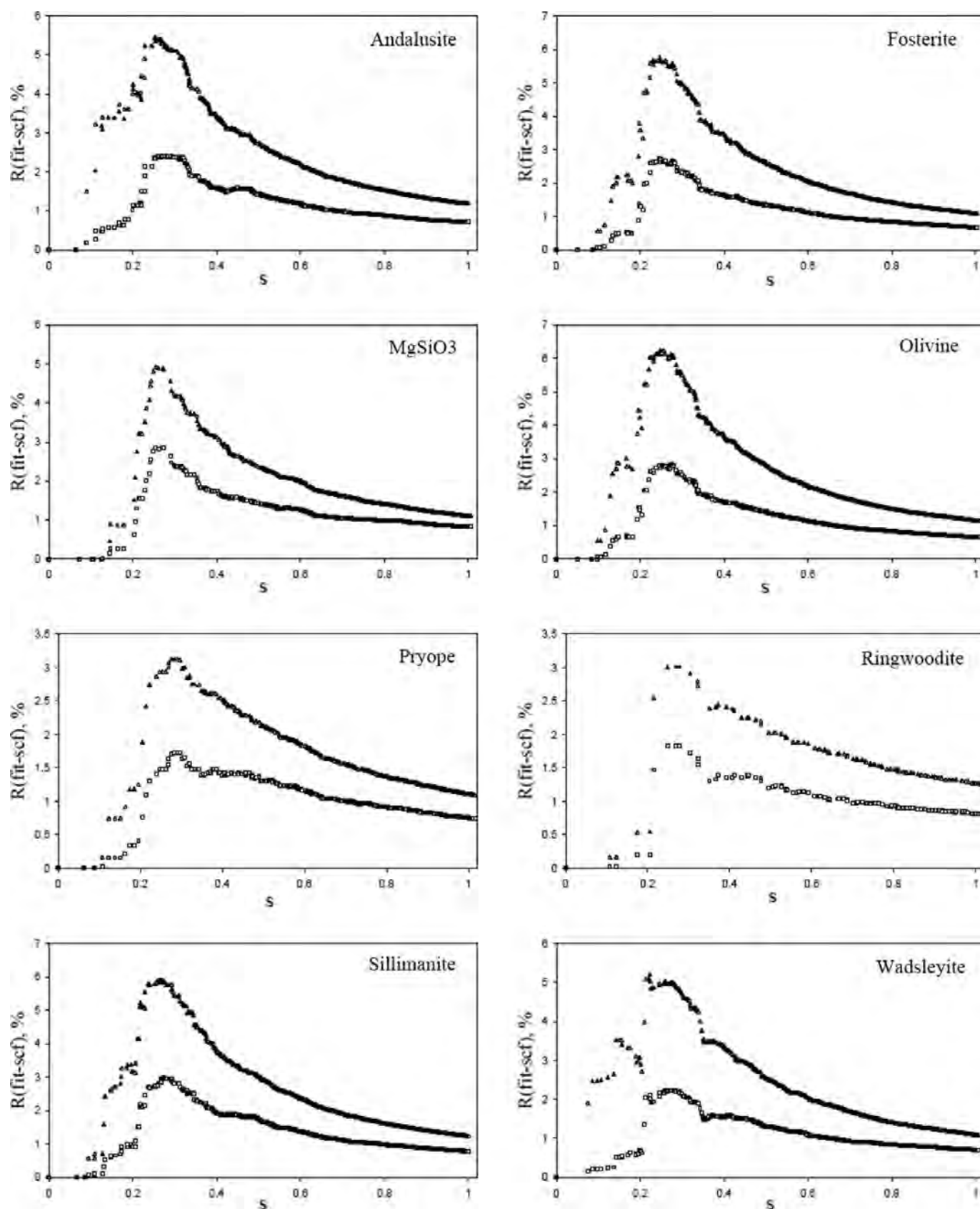


Figure 2
 $R(\text{fit-scf})$ for X-ray structure factors (squares) and electron structure factors (triangles). The unit of s is \AA^{-1} .

Table 3

Standard uncertainty (σ) for images and difference images simulated using JEOL 2200FS-AC (C_c -limited) parameters.

		$\sigma(\text{fit})$	$\sigma(\text{fit-sup}), \sigma(\text{fit-sup})/\sigma(\text{fit})$	$\sigma(\text{fit-scf}), \sigma(\text{fit-scf})/\sigma(\text{fit})$	$\sigma(\text{sup-scf}), \sigma(\text{sup-scf})/\sigma(\text{fit})$
Al ₂ SiO ₅ (andalusite)	[001]	0.23	0.0018, 0.76%	0.020, 8.6%	0.022, 9.3%
	[010]	0.26	0.0020, 0.79%	0.021, 8.2%	0.023, 8.8%
	[100]	0.29	0.0017, 0.58%	0.017, 5.9%	0.019, 6.4%
Mg ₂ SiO ₄ (forsterite)	[001]	0.21	0.00084, 0.39%	0.012, 5.5%	0.012, 5.5%
	[010]	0.20	0.0040, 0.84%	0.037, 7.6%	0.040, 8.3%
	[100]	0.19	0.0016, 0.82%	0.026, 14%	0.027, 14%
MgSiO ₃ (perovskite)	[001]	0.17	0.0017, 0.98%	0.011, 6.5%	0.012, 7.2%
	[010]	0.35	0.0019, 0.54%	0.017, 4.8%	0.018, 5.2%
	[100]	0.19	0.0019, 1.0%	0.014, 7.6%	0.016, 8.3%
Mg ₂ SiO ₄ (olivine)	[001]	0.21	0.00082, 0.39%	0.013, 5.9%	0.013, 6.0%
	[010]	0.21	0.0020, 0.93%	0.022, 10%	0.023, 11%
	[100]	0.20	0.0016, 0.80%	0.025, 13%	0.026, 13%
Al ₂ Mg ₃ Si ₃ O ₁₂ (pyrope)	[001]	0.59	0.0029, 0.49%	0.012, 2.1%	0.013, 2.3%
Mg ₂ SiO ₄ (ringwoodite)	[001]	0.51	0.0030, 0.59%	0.023, 4.4%	0.026, 4.9%
Al ₂ SiO ₅ (sillimanite)	[001]	0.18	0.0019, 1.1%	0.019, 11%	0.021, 12%
	[010]	0.32	0.0022, 0.70%	0.025, 8.0%	0.027, 8.5%
	[100]	0.25	0.0013, 0.53%	0.012, 4.6%	0.013, 5.0%
Mg ₂ SiO ₄ (wadsleyite)	[001]	0.49	0.0050, 1.0%	0.022, 4.5%	0.027, 5.5%
	[010]	0.25	0.0024, 0.97%	0.025, 9.8%	0.026, 10%
	[100]	0.64	0.0061, 0.96%	0.063, 9.8%	0.068, 11%

different microscopes. The first was for a (slightly older) conventional high-resolution instrument, which can reach a resolution of about 2.0 Å. The resolution limit of an electron microscope is roughly given by (Smith, 1997)

$$0.66(C_s \lambda^3)^{1/4}, \quad (3)$$

where C_s is the spherical aberration and λ the wavelength of incident electron beams. Therefore, it is possible to reach a sub-Å limit by correcting the spherical aberration to near zero or even negative values, which can be achieved by using in the microscope multipole elements such as quadrupoles, hexapoles and octupoles (Rose, 1990; Krivanek *et al.*, 1999). We also simulated images with imaging parameters from a C_5 -limited aberration-corrected microscope with a negative spherical aberration (Scherzer, 1970) and a C_c -limited aberration-corrected microscope with a small spherical aberration (O’Keeffe, 2000). Table 2 lists all the parameters used in the image simulations. No attempt was made to include any inelastic scattering effects.

3. Results

3.1. Comparison of calculated structure factors

We will discuss first the overall trends as a function of scattering angle; the effects of choosing different zone axes are more apparent in the imaging results, which will be described later. As shown in Table 1, our eight selected oxides are all somewhat ionic compounds. Compared with covalent bonds, ionic bonds result in larger charge redistribution which is not included in $F_{\text{fit}}^x, F_{\text{fit}}^e, F_{\text{sup}}^x$ and F_{sup}^e . To provide a summary of the differences, we found that a cumulative R factor defined by

$$R(1 - 2, s) = \frac{\sum_{s' \leq s} |f_1(s') - f_2(s')|}{\sum_{s' \leq s} |f_2(s')|} \quad (4)$$

gave a good overview. Fig. 1 shows $R(\text{fit-sup})$ factors for electron (triangles) and X-ray (squares) structure factors. All eight plots have similar behavior and in none of them does $R(\text{fit-sup})$ exceed 1%. Since both F_{fit}^x and F_{sup}^x are calculated from a superposition of atomic charge densities, there are no obvious differences between them. Theoretically, the atomic charge densities might be a little different when exchange and correlation potentials are treated in different schemes. Note that the five Gaussian parameters are fitted using the charge density from multiconfiguration Dirac–Fock wavefunctions (MCDF), where correlation effects are included whereas F_{sup}^x is calculated from relativistic Dirac–Slater wavefunctions with a GGA exchange–correlation potential. As shown in Fig. 1, the

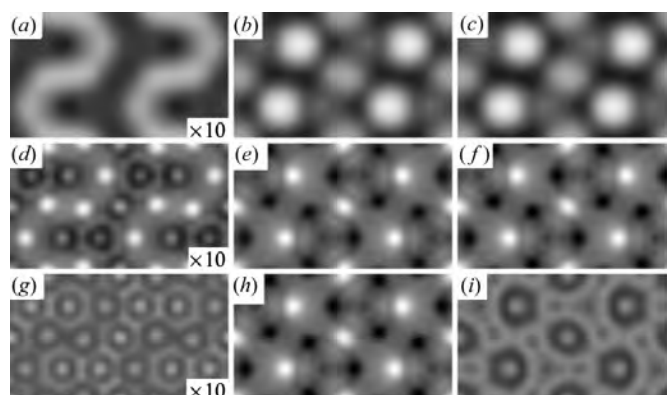


Figure 3 Difference images for forsterite [001]. (a), (b) and (c) are $I(\text{fit-sup})$, $I(\text{fit-scf})$ and $I(\text{sup-scf})$ with H9000 microscope parameters. (d), (e) and (f) are $I(\text{fit-sup})$, $I(\text{fit-scf})$ and $I(\text{sup-scf})$ under the aberration-correction (C_5 -limited) condition. (g), (h) and (i) are $I(\text{fit-sup})$, $I(\text{fit-scf})$ and $I(\text{sup-scf})$ under the aberration-correction (C_c -limited) condition. The contrast of $I(\text{fit-sup})$ images, (a), (d) and (g), is enhanced by a scaling factor of 10. The overall contrast range is -0.05698 to 0.08081 , normalized to unity for the mean intensity without a specimen.

exchange-correlation effects only lead to a change of about 0.25–0.5% in the 0–1 Å⁻¹ region.

Of more interest is the comparison with the DFT calculated results. Fig. 2 shows $R(\text{fit-scf})$. It is evident that for both X-rays and electrons the differences reach their maxima in the 0.2–0.3 Å⁻¹ region corresponding to spatial frequencies of 0.4 to 0.6 Å⁻¹, which is the short-range-bonding regime. As expected, bonding has almost no effect in the core region; the $R(\text{fit-scf})$ value is only about 1–2% for both X-rays and electrons at high scattering angles. In the 0–0.4 Å⁻¹ bonding region, $R(\text{fit-scf})$ for X-rays is typically about 2–3% and two to three times this for electrons.

As discussed before, the discrepancy between F_{fit} and F_{sup} is very small. Apparently, $R(\text{sup-scf})$ is similar to $R(\text{fit-scf})$ (see Supplementary Materials).¹ The same exchange-correlation potential was used for F_{sup} and F_{scf} . The $R(\text{sup-scf})$ factor only measures the difference due to crystal bonding; while the $R(\text{fit-scf})$ factor is affected not only by crystal bonding but also by exchange-correlation effects.

3.2. Image simulations with F_{fit}^e , F_{sup}^e and F_{scf}^e

Image simulations were performed along different zone axes. We used image difference maps to understand the effects of charge redistribution with the standard uncertainty (σ) of a gray image used as a quantitative measure of the contrast (see Table 3 and Supplementary Materials). It is evident that images simulated from F_{fit}^e and F_{sup}^e are almost identical with the difference between their standard uncertainties less than 2%. However, when the images with either of these are compared to the DFT results, the difference is 5–10 times larger. Typical difference images are shown in Fig. 3 for forsterite [001]. Although the conventional H9000 microscope does not reach Å resolution, there are still detectable charge redistribution effects. The aberration-corrected microscope can image more charge redistribution details and the C_c -limited condition is better than the C_s -limited condition.

3.3. Difference image contrast due to charge redistribution

To understand the changes in more detail, we will consider two examples. Both images are the differences between $I(\text{sup})$ and $I(\text{scf})$, generated under C_c -limited aberration-corrected conditions. Fig. 4(a) and Fig. 5(a) show the $I(\text{sup-scf})$ images for forsterite [001] and ringwoodite [001], respectively. There are three types of spots in Fig. 4(a), a bright spot 1, a dark spot 2 and a dark spot 3. There is only one kind of bright spot 4 and one kind of dark spot 5 in Fig. 5(a). Here we propose a simple method to interpret the image contrast.

Electrons are scattered by the electrostatic potential, which is the Coulomb potential of the nucleus screened by the electrons. When neutral atoms form an oxide, charge redistribution takes place and there is some charge transfer:

¹ $R(\text{sup-scf})$ graphs for X-ray and electron structure factors and tables of standard uncertainties for images and difference images using JEOL 2200FS-AC (C_s -limited) and H9000 parameters are available from the IUCr electronic archives (Reference: LC5043). Services for accessing these data are described at the back of the journal.

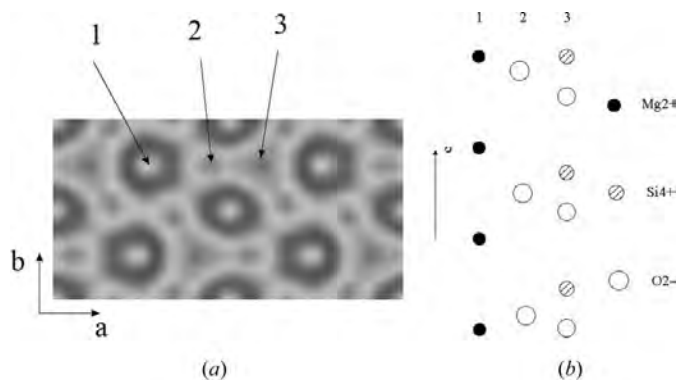


Figure 4 (a) $I(\text{sup-scf})$ for forsterite [001] and (b) its corresponding atomic columns.

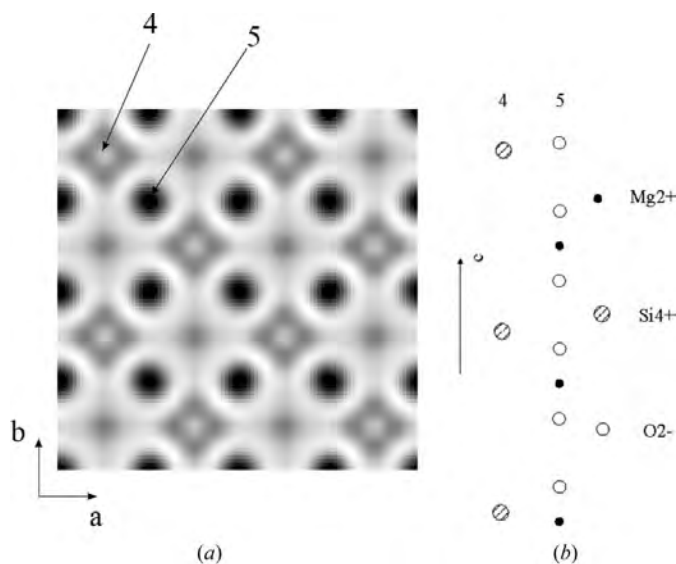


Figure 5 (a) $I(\text{sup-scf})$ for ringwoodite [001] and (b) its corresponding atomic columns.

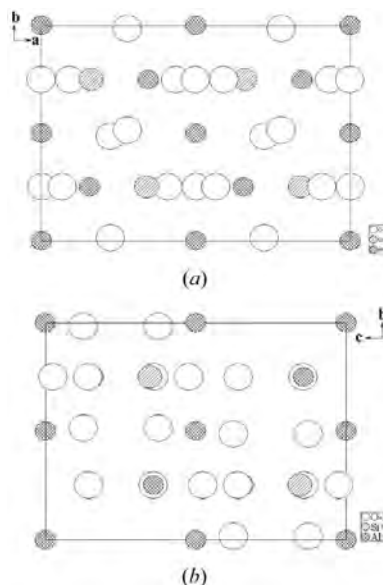
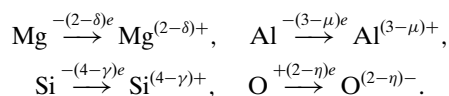


Figure 6 Alignments of atom columns of sillimanite (a) [001] and (b) [100].



Mg, Al, Si and O are usually not fully oxidized into Mg^{2+} , Al^{3+} , Si^{4+} and O^{2-} , but we will use this notation here for simplicity. Along the [001] direction in forsterite, there are three kinds of atomic columns, as shown in Fig. 4(b). Column 1 is composed only of Mg^{2+} cations whereas column 2 is composed only of O^{2-} anions. Finally, column 3 consists of alternating Si^{4+} cations and O^{2-} anions. Along column 1, all the Mg-atom columns become more positive on charge redistribution. For column 2, the electron densities around O-atom sites increase; consequently, the nuclear Coulomb potential is better screened. Comparing the difference image Fig. 4(a) with the crystal structure, we can assign atomic columns to spot 1 and spot 2, respectively. The corresponding spot for column 3 is small and dark. Although the potential of the Si atom in the column becomes more positive after charge redistribution, the silicon bonding has a substantial covalent character and the decrease in the potential associated with the O atoms is even

larger. Therefore, the total potential of column 3 is smaller after charge redistribution. It is interesting that the effect of the anions is always larger than the effect of the cations. In all the images we simulated, we found that the total projected potential decreases after charge redistribution for a column with mixed cations and anions, although we acknowledge that there may well be other cases that would go the other way. Another example is the $I(\text{sup-scf})$ for ringwoodite [001]. As shown in Fig. 5(a), only two kinds of spots, 4 and 5, exist in the difference image. Similarly, spot 4 and spot 5 can be assigned to column 4 and column 5 in Fig. 5(b). Column 4 has only Si^{4+} cation sites and results in a bright spot in the image. An even higher ratio of O-atom sites is seen along the column 5 when compared with column 3, resulting in a diffuse dark spot.

3.4. Alignment of atom columns and its effect on difference image contrast

The difference image contrast can be affected by a number of variables, such as cell size, alignment of atomic columns as well as the imaging parameters (see Table 3 and Supplementary Materials).

The most significant effect is the alignment of atom columns, which is directly related to charge transfer. To eliminate other effects, we compared two simulated images with the same cell sizes using the same imaging parameters. Notice that the sillimanite [001] and [100] images have almost the same sizes, $7.681 \times 5.777 \text{ \AA}$ and $7.488 \times 5.777 \text{ \AA}$, respectively (Fig. 6). However, the ratios of $\sigma(\text{fit-scf})/\sigma(\text{fit})$ are very different with sillimanite [001] two or three times larger than that for sillimanite [100]. As shown in Fig. 6(a), cations and anions are aligned along the [001] direction, whereas, along the [100] direction, some Al^{3+} cations and O^{2-} anions are in the same columns. In addition, all the Si^{4+} cations are aligned with O^{2-} anions in the same columns. Therefore, any increase in site potentials for Al^{3+} and Si^{4+} cations is cancelled by O^{2-} anions. The

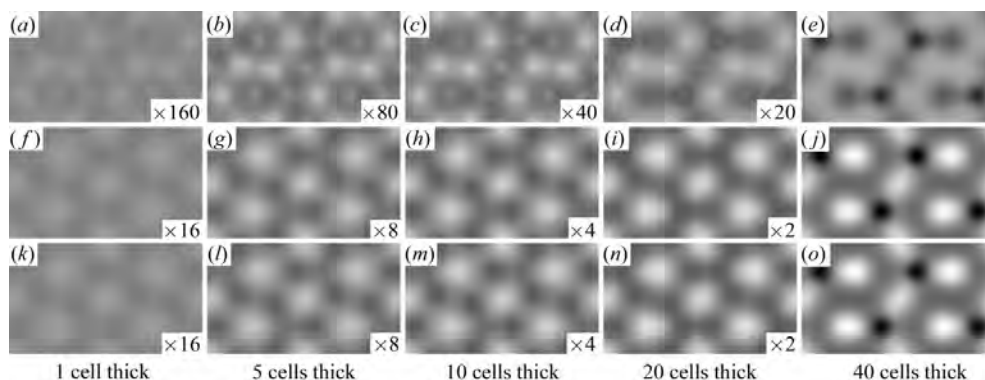


Figure 7 Difference images of forsterite [001] under JEOL 2200FS aberration-corrected (C_s -limited) microscope conditions. (a)–(e) are $I(\text{fit-sup})$ images. (f)–(j) are $I(\text{fit-scf})$ images. (k)–(o) are $I(\text{sup-scf})$ images. The thickness is from 1 to 40 unit cells. The scaling factor of image contrast is indicated at bottom right. The overall contrast range is -0.1826 to 0.1540 , normalized to unity for the mean intensity without a specimen.

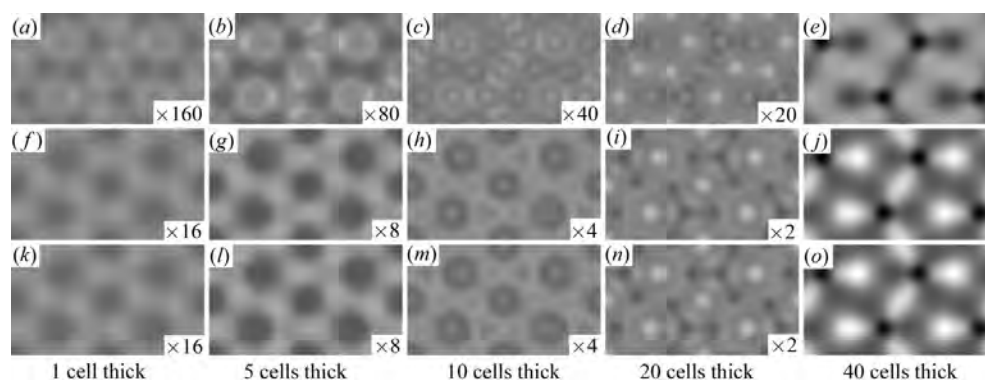


Figure 8 Difference images of forsterite [001] under JEOL 2200FS aberration-corrected (C_c -limited) microscope conditions. (a)–(e) are $I(\text{fit-sup})$ images. (f)–(j) are $I(\text{fit-scf})$ images. (k)–(o) are $I(\text{sup-scf})$ images. The thickness is from 1 to 40 unit cells. The scaling factor of image contrast is indicated at bottom right. The overall contrast range is -0.08882 to 0.08443 , normalized to unity for the mean intensity without a specimen.

remaining images also exhibit this effect. For enhanced charge-density image contrast, the atoms should be aligned in different columns as much as possible, and cations and anions should not be in the same column. Note that the zone axes that maximize the difference in image contrast will also be those that will be most sensitive in a diffraction experiment.

3.5. Thickness and defocus effects on difference images

In the previous section, we discussed how to use difference images to study charge transfer qualitatively. To further illustrate the approach, we should also evaluate the effects of other imaging parameters. Here we will only discuss thickness and defocus effects. [We found that the effects of vibration and drift ($<1 \text{ \AA}$) were small and, in difference images, could be neglected.]

In HREM simulations, the thinner the specimen, the easier it is to interpret the images in most cases. However, the effect of bonding is small and can be very hard to observe if the specimen is too thin. Figs. 7 and 8 are simulated images for forsterite with thicknesses ranging from 1 to 40 unit cells along the [001] direction. The $I(\text{fit-sup})$ images, which are difference images due to different exchange-correlation potentials, show

no consistent indications of charge transfer. For the C_5 -limited condition, the optimum thickness for observing charge transfer in forsterite [001] is about from 5 to 10 cells thick. For the C_c -limited condition, it is from 10 to 20 cells thick.

Figs. 9 and 10 are through-focal series of images for forsterite [001] with defoci ranging from -3.0 to 3.0 Sch [$1 \text{ Sch} = 1.2(C_s\lambda)^{1/2}$]. For the C_5 -limited conditions, as shown in Fig. 9, three kinds of spots can be resolved in the images with defoci from 0.0 to 35 \AA , where bright spots occur at cation columns and dark spots at anion and mixed-ion columns. For the C_c -limited conditions, a broader window of defoci exists from -35 to 35 \AA within which the three 'charge-transfer' spots can be resolved.

4. Discussion

From calculations of three different sets of structure factors and comparison of their effects on simulations, we can conclude that the structure factors from a linear combination of different atomic charge densities are almost the same. We acknowledge that it is still reasonable to use atomic charge densities for most structure-factor calculations. In terms of the

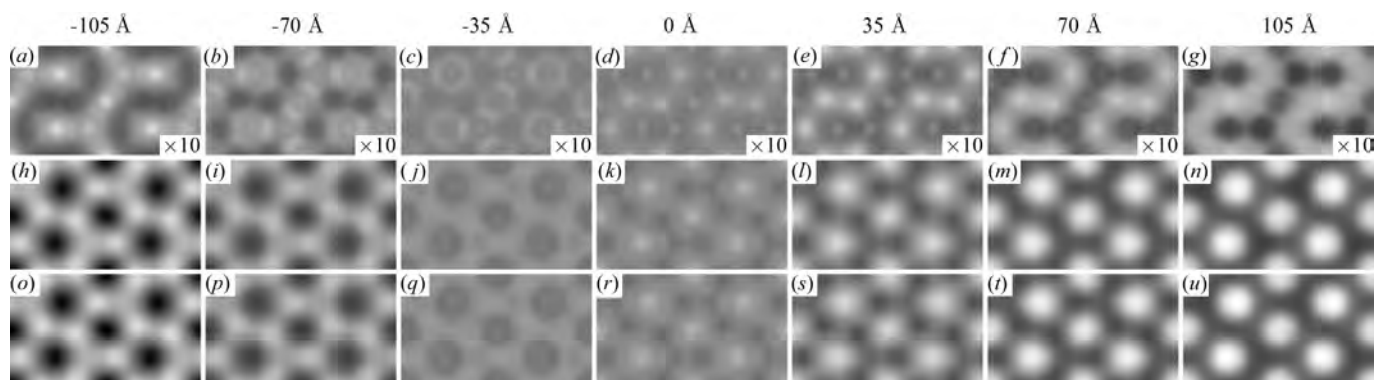


Figure 9

Difference images of forsterite [001] under JEOL 2200FS aberration-corrected (C_5 -limited) microscope conditions with different focus. (a)–(g) are $I(\text{fit-sup})$ images. (h)–(n) are $I(\text{fit-scf})$ images. (o)–(u) are $I(\text{sup-scf})$ images. The image contrast of $I(\text{fit-sup})$ images is enhanced by a scaling factor of 10. The overall contrast range is -0.03983 to 0.03450 , normalized to unity for the mean intensity without a specimen.

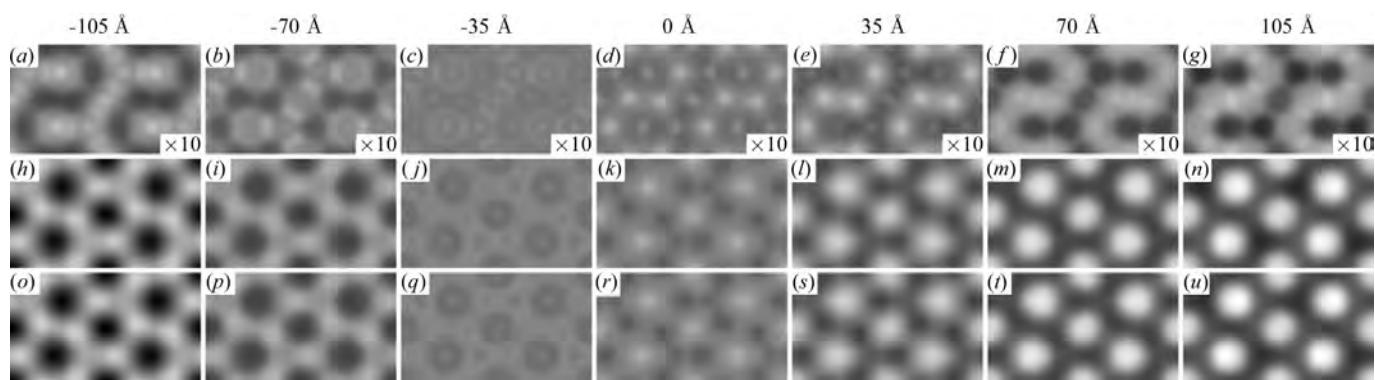


Figure 10

Difference images of forsterite [001] under JEOL 2200FS aberration-corrected (C_c -limited) microscope conditions with different focus. (a)–(g) are $I(\text{fit-sup})$ images. (h)–(n) are $I(\text{fit-scf})$ images. (o)–(u) are $I(\text{sup-scf})$ images. The image contrast of $I(\text{fit-sup})$ images is enhanced by a scaling factor of 10. The overall contrast range is -0.03433 to 0.03529 , normalized to unity for the mean intensity without a specimen.

effects of bonding on structure factors, we find that these are small for X-rays and rather larger for electrons as expected and consistent with the published literature. While the effects are small, there are certain differences in images due to charge redistribution which might be detectable with a C_c -limited aberration-corrected microscope. Alignment of the atom columns is shown to have a significant effect on how strong the effects are. Something that we would not have previously expected is that anions seem to lead to larger effects than cations.

One important question is whether these effects are detectable in images with current electron microscopes. To be able to quantitatively detect differences of about 10% in the overall contrast requires accuracy at about the 1% level or better. Using standard Poisson statistics, this requires on the order of 10^4 electrons pixel^{-1} , which is certainly well within the range of current CCD detectors.

Of course, in practice it will not be quite as easy as obtaining very good quality images with a high total number of counts per pixel. We have neglected inelastic scattering, which is going to be a relatively small effect for a thin sample but may need to be considered. In principle, there is a potential change due to virtual inelastic scattering, but this is of the order of 10^{-5} – 10^{-4} (Rez, 1978), which is much smaller than bonding effects (10^{-2}). Although image contrast is often less than theory predicts, the so-called Stobbs factor (Hytch & Stobbs, 1994; Boothroyd, 1998), with care and perhaps the use of electron holography we believe this problem will soon be overcome. From our practical experience with UHV-HREM, we have often observed that a sample with a flat surface and a low density of point defects shows a much lower diffuse scattering background than normal samples (Storey *et al.*, 1995) and this is probably at least as important if not more so than reducing or eliminating inelastic scattering contributions. These issues fall outside the scope of this paper which was more to analyze whether or not one can observe differences in the relative contrast of different atomic columns in an image due to bonding effects.

The challenge for observing charge redistribution experimentally will almost certainly be making samples which are sufficiently well controlled (*e.g.* thickness, no amorphous contaminants or ion-beam damage, very flat) that the effects can be observed in a perfect region of the sample. Potentially easier experimentally (and certainly of more interest scientifically) would be to look at defects. Here, since one will have a local reference region, it may be much easier to analyze the results. We can predict that charge redistribution effects at defects will be of a comparable magnitude to those detailed herein; a more concrete analysis will be the subject of future work.

The authors would like to thank Dr Lan Yun Chang for providing imaging parameters for aberration-corrected microscopes. We acknowledge financial support from the Department of Energy under grant No. DE-FG02-01ER45945.

References

- Blaha, P., Schwarz, K., Madsen, G. K. H., Kvasnicka, D. & Luitz, J. (2001). *WIEN2k, an Augmented Plane Wave + Local Orbitals Program for Calculating Crystal Properties*. Vienna University of Technology.
- Blaha, P., Schwarz, K., Sorantin, P. & Trickey, S. B. (1990). *Comput. Phys. Commun.* **59**, 399–415.
- Boothroyd, C. B. (1998). *J. Microsc.* **90**, 99–108.
- Cowley, J. M. & Moodie, A. F. (1957). *Acta Cryst.* **10**, 609–619.
- Doyle, P. A. & Turner, P. S. (1968). *Acta Cryst.* **A24**, 390–397.
- Friis, J., Madsen, G. K. H., Larsen, F. K., Jiang, B., Marthinsen, K. & Holmestad, R. (2003). *J. Chem. Phys.* **119**, 11359–11366.
- Gjonnes, K. & Boe, N. (1994). *Micron*, **25**, 29–44.
- Goodman, P. & Moodie, A. F. (1974). *Acta Cryst.* **A30**, 280–290.
- Grant, I. P., McKenzie, B. J., Norrington, P. H., Mayers, D. F. & Pyper, N. C. (1980). *Comput. Phys. Commun.* **21**, 207–231.
- Holmestad, R. & Birkeland, C. R. (1998). *Philos. Mag.* **A77**, 1231–1254.
- Holmestad, R., Birkeland, C. R., Marthinsen, K., Hoier, R. & Zuo, J. M. (1999). *Microsc. Res. Tech.* **46**, 130–145.
- Hytch, M. J. & Stobbs, W. M. (1994). *Microsc. Microanal. Microstruct.* **5**, 133–151.
- Jiang, B., Zuo, J. M., Chen, Q. & Spence, J. C. H. (2002). *Acta Cryst.* **A58**, 4–11.
- Jiang, B., Zuo, J. M., Jiang, N., O’Keeffe, M. & Spence, J. C. H. (2003). *Acta Cryst.* **A59**, 341–350.
- Krivanek, O. L., Dellby, N. & Lupini, A. R. (1999). *Ultramicroscopy*, **78**, 1–11.
- Liberman, D. A., Cromer, D. T. & Waber, J. T. (1971). *Comput. Phys. Commun.* **2**, 107–113.
- Madsen, E. N., Fox, A. G. & O’Keeffe, M. A. (1992). *International Tables for Crystallography*, Vol. C, pp. 476–511. Dordrecht: Kluwer Academic Publishers.
- Nuechter, W., Weickenmeier, A. L. & Mayer, J. (1998). *Phys. Status Solidi A*, **166**, 367–379.
- O’Keeffe, M. A. (2000). *Microsc. Microanal.* **6**, 1036–1037.
- Peng, L. M. & Cowley, J. M. (1988). *Acta Cryst.* **A44**, 1–5.
- Perdew, J. P., Burke, K. & Wang, Y. (1996). *Phys. Rev. B*, **54**, 16533–16539.
- Rez, D., Rez, P. & Grant, I. (1994). *Acta Cryst.* **A50**, 481–497.
- Rez, P. (1978). *Acta Cryst.* **A34**, 48–51.
- Rose, H. (1990). *Optik (Stuttgart)*, **85**, 19–24.
- Saunders, M., Fox, G. & Midgley, P. A. (1999). *Acta Cryst.* **A55**, 471–479.
- Saunders, M., Midgley, P. A. & Vincent, R. (1995). *Institute of Physics Conference Series*, No. 147, pp. 125–128. Bristol: IOP.
- Saunders, M., Midgley, P., Vincent, R. & Steeds, J. (1996). *J. Electron Microsc.* **45**, 11–18.
- Scherzer, O. (1970). *Ber. Buns. Ges. Phys. Chem.* **74**, 1154–1167.
- Smith, D. J. (1997). *Rep. Prog. Phys.* **60**, 1513–1580.
- Storey, B. G., Kirk, M. A. & Marks, L. D. (1995). *Physica (Utrecht)*, **C246**, 46–54.
- Tsuda, K., Ogata, Y., Takagi, K., Hashimoto, T. & Tanaka, M. (2002). *Acta Cryst.* **A58**, 514–525.
- Waasmaier, D. & Kirfel, A. (1995). *Acta Cryst.* **A51**, 416–431.
- Wu, L. J., Zhu, Y. M., Vogt, T., Su, H. B., Davenport, J. W. & Taftø, J. (2004). *Phys. Rev. B*, **69**, 064501–1–8.
- Zheng, J. C., Zhu, Y., Wu, L. & Davenport, J. W. (2005). *J. Appl. Cryst.* **38**, 648–656.
- Zuo, J. M. (2004). *Rep. Prog. Phys.* **67**, 2053–2103.
- Zuo, J. M., Blaha, P. & Schwarz, K. (1997). *J. Phys. Condens. Matter*, **9**, 7541–7561.
- Zuo, J. M., Kim, M., O’Keeffe, M. & Spence, J. C. H. (1999). *Nature (London)*, **401**, 49–52.
- Zuo, J. M. & Spence, J. C. H. (1991). *Ultramicroscopy*, **35**, 185–196.
- Zuo, J. M., Spence, J. C. H. & O’Keeffe, M. (1988). *Phys. Rev. Lett.* **61**, 353–356.